Anisotropic coercivity and the effects of interlayer exchange coupling in CoFeB/FeRh bilayers

Chenyu Zhang,[1,2] Yali Xie,[3] Qingfeng Zhan,[4,*] and Yong Hu[1,2,†]

[1]*Department of Physics, College of Sciences, Northeastern University, Shenyang 110819, China*

[2]*State Key Laboratory of Rolling and Automation, Northeastern University, Shenyang 110819, China*

[3]*Key Laboratory of Magnetic Materials and Devices, Ningbo Institute of Material Technology and Engineering, Chinese Academy of Sciences, Ningbo 315201, China*

[4]*Key Laboratory of Polar Materials and Devices (MOE) and State Key Laboratory of Precision Spectroscopy, School of Physics and Electronic Science, East China Normal University, Shanghai 200241, China*

(Received 24 July 2020; revised 8 January 2021; accepted 8 January 2021; published 27 January 2021)

In an amorphous CoFeB layer, coercivity becomes anisotropic with fourfold symmetry when the CoFeB layer exchange couples to an FeRh layer. The angular dependence of coercivity of the CoFeB layer coincides with the in-plane easy-axis direction of the FeRh layer and experiences a 45° shift with the occurrence of a metamagnetic phase transition of the FeRh layer from antiferromagnetism at room temperature to ferromagnetism at 400 K. The intriguing phenomena are well reproduced by our unbiased Monte Carlo simulation. The interfacial exchange and anisotropy energies, as well as the interfacial magnetization in the CoFeB/FeRh bilayer, are disentangled to demonstrate the strong dependence of the imprinting of anisotropy in the CoFeB layer on the interfacial exchange coupling. The evolution of the easy-axis direction of the induced anisotropy arises from the reconstruction of the interfacial exchange energy profile accompanied with the change of the magnetic state of FeRh, which governs the magnetization reversal of the CoFeB layer at both branches. Moreover, the imprinting is further applicable for the uniaxial magnetocrystalline anisotropy. This work not only presents the possibility of directly duplicating anisotropy between dissimilar materials, but it also provides a powerful tool to probe the hidden magnetic structures and/or the properties of materials that have weak magnetism, such as antiferromagnetic materials.

DOI: 10.1103/PhysRevB.103.014445

I. INTRODUCTION

When two or more dissimilar materials with different long-range magnetic orderings and/or functionalities are combined, it may give rise to new interfacial properties, such as the exchange bias/spring effect [1–4] and the magnetic proximity effect [5–8]. The research in this area has become an important aspect of modern information technology, since one can expect various novel properties in such composite materials that are not present in constituent materials. The continued progress is highly advantageous for the development of magnetic read-heads, high-density magnetic storage media, etc. [9]. Nevertheless, there may be lattice mismatch, strain, and defects at interfaces, resulting in different magnetic structures at the vicinity of the interface from the bulk [10], as well as complex crystallographic and magnetic reconstructions and relaxations at interfaces. Moreover, a precise determination of the structural and magnetic nature of the interface is often hindered by the difficulty of measuring the interface due to its low volume; in other words, it is challenging to extract the interfacial contributions from individual components. As a result, the challenges of understanding the physics behind the interface phenomena have promoted this technologically important area as a promising one both for theoreticians and experimentalists.

Magnetic anisotropy generally originates from the spin-orbit coupling and long-range dipolar interaction of magnetic moments [11–13], which determines the direction of a spontaneous magnetization vector with respect to the lattice axes. The spin-orbit coupling is responsible for intrinsic magnetocrystalline anisotropies such as uniaxial anisotropy in the case of a hexagonal crystal and cubic anisotropy in the case of a cubic one, while the dipolar interaction mainly contributes to shape anisotropy. The intrinsic anisotropy energies are usually in the range of 10^2–10^7 J m^{-3}, depending on the lattice symmetry; that is, the anisotropy energy in lowly symmetric lattices of magnetic ions is larger than that in highly symmetric lattices, such as Fe-Ni ($\sim 2 \times 10^2$ J m^{-3}) [14,15], Fe-Co ($\sim 10^4$ J m^{-3}) [16], Fe-Al ($\sim 10^4$ J m^{-3}) [16], magnetite ($\sim 2.5 \times 10^4$ J m^{-3}) [17], pure Fe ($\sim 5 \times 10^4$ J m^{-3}) [18], pure Ni ($\sim 8 \times 10^4$ J m^{-3}) [19], and a series of ferrites ($\sim 10^4$–10^5 J m^{-3}) [20–23]. Weak magnetic anisotropies are desired to minimize hysteresis losses, eddy current, and anomalous losses when maximizing permeability; on the contrary, strong magnetic anisotropies contribute to large amounts of magnetic hysteresis, with figures of merit including coercive force, remnant magnetization, and energy product [24]. Remarkably, different anisotropy energy levels suit different applications, therefore the development of methods to control anisotropy in materials can extend the materials' functionalities. A few studies have been reported showing that the anisotropy magnitude can be fine-tuned by annealing or

*Author to whom all correspondence should be addressed: qfzhan@phy.ecnu.edu.cn

†huyong@mail.neu.edu.cn

doping elements [13,25], and the anisotropy direction can also be precisely adjusted between in-plane and out-of-plane directions by changing the Co layer thickness in a Co/Pd superlattice [26,27].

Between two dissimilar magnetic components, the usual signature of magnetic proximity is that the component with a high ordering temperature could enhance the lower one [7,28], and many other interesting phenomena have also been presented, such as the enhancement of perpendicular magnetic anisotropy in Fe/Mn bilayers by incorporating an additional ultrathin Fe film [29], the enhancement of coercivity at temperatures far above the antiferromagnetic Néel temperature in Co/FeF_2 bilayers [30,31], and a directional exchange bias in the FeRh-based bilayers [32,33]. In the Fe/Mn bilayers, the magnetic ordering temperature in the Mn film was increased due to the magnetic proximity to the Fe underlayer, and thus the thermal stability of low-dimensional Mn film was promoted. A direct imaging of magnetic structures at interfaces was achieved by an element-specific x-ray magnetic circular dichroism (XMCD) measurement technique [31], and an enhanced coercivity in Co/FeF_2 bilayers was attributed to the detectably unpinned Fe uncompensated moments coupling with the Co layer. In Fe/FeRh bilayers, exchange bias was observed in the FeRh(111) plane while it was absent in the FeRh(001) plane [32]. On the other hand, a unidirectional anisotropy (exchange bias) constant up to 0.8 erg cm^{-2} has been reported at the FePt/FeRh(001) interface [33]. Remarkably, the magnetic proximity effect involving exchange bias usually arises from hard magnets with a large anisotropy, such as an antiferromagnet, which provides an additional energy well to capture the moments of soft magnets, e.g., an amorphous ferromagnet, CoFeB. Recent theoretical investigations based on micromagnetic calculation and Monte Carlo simulation [34–40] supported the idea that both the magnetic structure of the pinning layer at the interface and the domain walls parallel to the interface play a key role in the final interface magnetism.

In this work, the angular dependence of coercivity in the CoFeB/FeRh bilayer is systematically studied. The paper is organized as follows: In Sec. II, the experimental results of hysteresis loops as well as the extracted coercivity behaviors are summarized, which show that the FeRh magnetic anisotropy can be well imprinted on the coercivity behavior of the CoFeB layer with respect to the magnetizing direction, and the FeRh magnetic states at different temperatures can tune this angular dependence of coercivity. In Sec. III, a bilayer model containing the energy terms of magnetic anisotropies and exchange interactions is established, and its magnetically hysteretic behaviors are examined by means of the classical Monte Carlo method. The phenomena are reproduced and interpreted by our simulation in Sec. IV. The simulation results of magnetic energy variations with temperature and magnetizing direction elucidated that the induced anisotropy is stabilized and governed by interfacial exchange coupling. The final section is devoted to a summary and outlook.

II. SUMMARY OF EXPERIMENTS

The $Co_{40}Fe_{40}B_{20}$(CoFeB)/FeRh bilayer with an FeRh thickness of 30 nm and a CoFeB thickness of 10 nm was deposited on the commercial (001)-oriented MgO substrate [see Fig. 1(a)] in a magnetron sputtering system with a base pressure below 1.0×10^{-8} Torr. At first, the substrate was annealed at 500 °C for 1 h in a vacuum chamber. Then, the FeRh layer was grown at a temperature of 530 °C, followed by annealing at 650 °C for 1 h. Finally, the CoFeB layer was deposited on the top of the FeRh layer after cooling the sample down to room temperature. Prior to being taken out of the vacuum chamber, the sample was capped by a 3 nm Ta layer to avoid oxidation. The film thicknesses were controlled by deposition time, which have been calibrated by x-ray reflectivity (XRR). The magnetic switching processes were measured by using a magneto-optical Kerr effect (MOKE) setup. Prior to MOKE measurements, the sample was heated to 400 K, which is above the antiferromagnetic-to-ferromagnetic phase transition temperature, and then cooled down to 300 K with an external magnetic field of 2 T along the MgO[100] direction in a magnetic property measurement system (MPMS, Quantum Design). The magnetic anisotropy was quantitatively determined by a ferromagnetic resonance (FMR) spectroscopy at the microwave frequency of 9.5 GHz.

Figure 1(b) shows the MOKE loops of the CoFeB(10 nm)/FeRh(30 nm) bilayer measured at room temperature in different in-plane magnetic field orientations (φ) with respect to the MgO[100] direction. The coercivity H_{cI} of 73 Oe at $\varphi = 0^\circ$ is observed, which is much larger than $H_c = 15$ Oe in a single CoFeB layer, indicating the existence of an interfacial exchange coupling between CoFeB and FeRh layers. Meanwhile, a two-step magnetic transition of ascending branch emerges at $\varphi = 20^\circ$ and 40°, indicating that the magnetization along the lateral directions can be detectable [41–44]. The angular dependence of H_{cI} and H_{cII} in the CoFeB(10 nm)/FeRh(30 nm) bilayer at room temperature indicates a distinct fourfold symmetry about the in-plane MgO[100] and MgO[010] directions, as depicted in Fig. 1(c). However, the CoFeB layer with an amorphous crystal structure should not possess any intrinsic fourfold magnetocrystalline anisotropy.

To quantitatively analyze the induced fourfold magnetic anisotropy in the CoFeB layer, the FMR derivative absorption spectra for the CoFeB(10 nm)/FeRh(30 nm) bilayer are detected at various φ at room temperature, as presented in Fig. 2(a). The resonance field exhibits four minimum values at $\varphi = 0^\circ$, 90°, 180°, and 270°, corresponding to the FeRh⟨110⟩ easy-axis directions, that is, an induced fourfold magnetic anisotropy in the CoFeB layer overlaps the FeRh intrinsic anisotropy, when the FeRh layer is in an antiferromagnetic (AFM) state at room temperature. Remarkably, as the temperature of the magnetic phase transition is approaching and the FeRh layer becomes ferromagnetic (FM), H_r along the FeRh⟨100⟩ direction becomes minimal, which indicates that the easy-axis directions are shifted by 45°, as shown in Fig. 2(b).

III. MODELING OF EXPERIMENTS

To interpret the experimental findings shown above, a coarse model, which consists of $100 \times 100 \times 22$ atoms placed on the nodes of a simple-cubic lattice, is used, where two-monolayer (ML) CoFeB layers are on the top of 20-ML FeRh

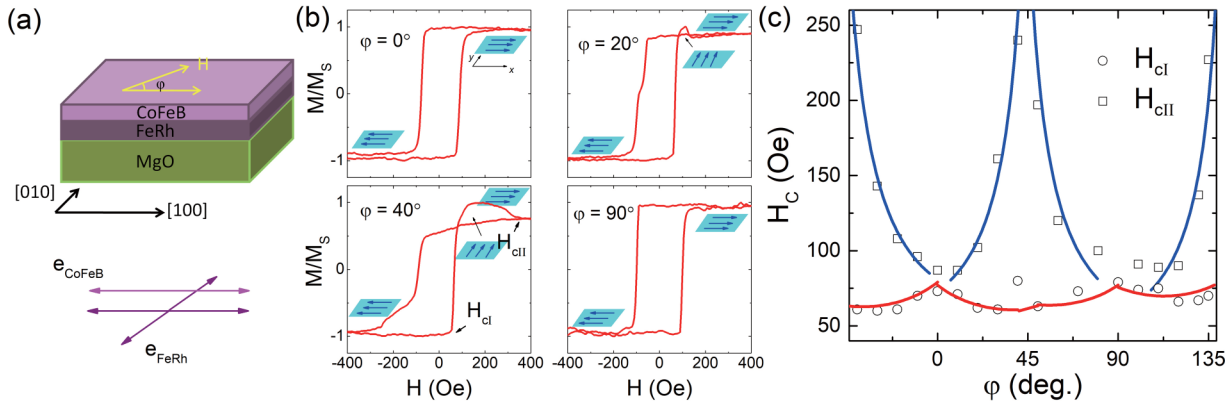

FIG. 1. (a) Sample structure of the CoFeB/FeRh bilayer grown on the MgO(001) substrate. The weak uniaxial anisotropy of the CoFeB layer and the strong in-plane fourfold anisotropy of the FeRh layer are shown in the bottom panel. (b) Typical MOKE loops of the CoFeB(10 nm)/FeRh(30 nm) bilayer in selected magnetizing directions at room temperature, where φ is designated as an angle between the in-plane measuring field and MgO[100] directions, $H_{\rm cI}$ and $H_{\rm cII}$ are weak- and strong-field coercivities at ascending branches, and blue arrows indicate the moment orientations of the CoFeB layer. (c) $H_{\rm cI}$ and $H_{\rm cII}$ as a function of φ.

layers. In the film plane, periodic boundary conditions are considered while open boundary conditions are set along the film normal. In the presence of an external magnetic field, the Hamiltonian can be written as

$$\begin{aligned}\mathcal{H} = &- \sum_{i\in\text{CoFeB}} k_1\left(\mathbf{s}_i\cdot\hat{e}_{k_1}^{\rm UA}\right)^2 - \sum_{\langle ij\in\text{CoFeB}\rangle} j_1\mathbf{s}_i\cdot\mathbf{s}_j \\ &- \sum_{i\in\text{FeRh}} k_2\left(\mathbf{s}_i\cdot\hat{e}_{k_2}^{\rm CA}\right)^4 - \sum_{\langle ij\in\text{FeRh}\rangle} j_2\mathbf{s}_i\cdot\mathbf{s}_j \\ &- \sum_i H(\mathbf{s}_i\cdot\hat{e}_H) - \sum_{\langle i\in\text{CoFeB},\, j\in\text{FeRh}\rangle} j_{12}\mathbf{s}_i\cdot\mathbf{s}_j, \qquad (1)\end{aligned}$$

where $\mathbf{s}_i$ denotes the unit vector of the ith atom moment, and $\hat{e}$ denotes the unit vector along the easy-axis or magnetic-field direction. The first two terms are anisotropy and exchange energies in the CoFeB layer; a weak uniaxial anisotropy (UA) is assumed, and the angular brackets denote the summations over the nearest neighbors only. The next two terms give the anisotropy and exchange energies of the FeRh layer, where a strong cubic anisotropy (CA) is considered unless stated otherwise. The last two terms present the Zeeman and interfacial exchange energy contributions.

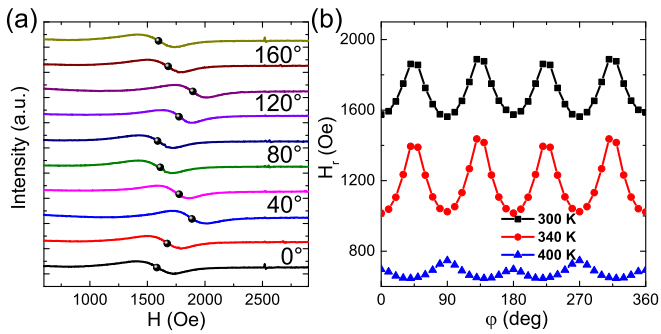

FIG. 2. (a) Typical FMR spectra measured in different field orientations (φ) for the CoFeB(10 nm)/FeRh(30 nm) bilayer at room temperature, where black dots indicate the resonance fields. (b) Typical angular dependence of resonance field H_r at selected temperatures.

For the amorphous CoFeB and epitaxially grown FeRh layers, the magnetic parameters $k_1 = 1.8\times10^2$ J m^{-3}, $j_1 =$ 10 meV at^{-1}, the saturation magnetization $M_{\rm S} = 1.2\times10^6$ A m^{-1}, $k_2 = 1\times10^7$ J m^{-3}, and $j_2 = \pm0.1\,j_1$ are used [45–47], i.e., the magnetic state of the FeRh layer is adjustable by $j_2 < 0$ and $j_2 > 0$, which represent the AFM and FM states, respectively. Furthermore, the easy-axis direction in the CoFeB layer is aligned with the magnetic field, i.e., $\hat{e}_{k_1}^{\rm UA} = \hat{e}_H$, while the easy-axis directions of the FeRh layer are fixed along the x and y axes. Finally, $j_{12} = j_1$ for simplicity. The bilayer with dimensions in the range of those experimentally investigated is far from the straightforward calculations. In other words, the determination of the spin structure of such a bilayer based on the investigation of its individual magnetic moments using Monte Carlo techniques becomes prohibitively time-consuming with present standard computational facilities. Therefore, in order to obtain the informative results such as magnetization in a model with much smaller sizes, the input magnetic parameters may be unrealistically large as compared to the real values presented above [48]. This issue can be solved to achieve an agreement between experiment and simulation if we resort to a scaling technique, which is based on an approximation of micromagnetism [49]. The detailed scaling process can be found in Refs. [49,50], and the scaling factor x is determined as 0.1362 by setting the lattice size scaling relation $x^{0.551} =$ [simulation value]/[real value] $= 1/3$ [49].

In the simulation, the initial state of the bilayer is magnetically disordered, and the system is annealed from 450 to 22.5 K in zero field. At a given temperature after (zero-) field-cooling, the magnetization hysteresis loop is recorded by cycling the magnetic field between 400 and −400 Oe. To study the role of the cooling process and the magnetizing direction, the cooling field ($H_{\rm FC} = 0.8$ or 2 T) may be applied and the magnetizing direction can vary from 0° to 355° with respect to the positive x-direction. To update the spin state, the Monte Carlo METROPOLIS algorithm is used. At each temperature or field, 2×10^4 Monte Carlo steps (MCSs)

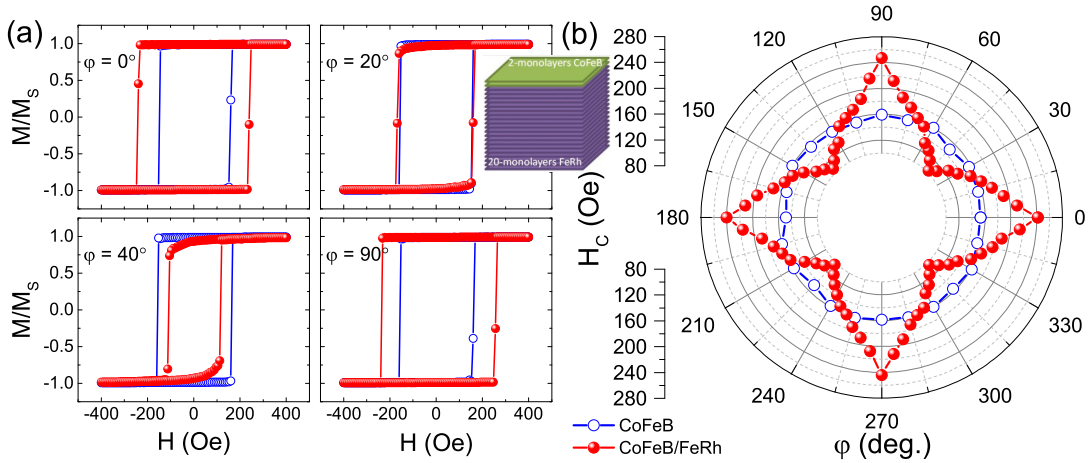

FIG. 3. (a) Calculated magnetization hysteresis loops at selected magnetizing directional angles with respect to the positive x-direction (φ) in CoFeB single layer (open symbol) and CoFeB/(FM) FeRh bilayer (solid symbol). (b) Calculated coercivity as a function of φ. The inset shows the model of CoFeB(2)/FeRh(20) bilayer, where numbers are in units of monolayers.

are performed with the first 10^4 MCSs thermally equilibrating the system, followed by another 10^4 MCSs to average the magnetization and magnetic energy quantities. The sweep rate is slow enough to guarantee quasiequilibrium, and the final simulation results are obtained after averaging the results obtained from 50 sets of independent initial states.

IV. NUMERICAL RESULTS

The results of the magnetization hysteresis loops in the CoFeB single layer and the CoFeB/FeRh bilayer at selected magnetizing directional angles (φ) are shown in Fig. 3(a). The loops of the CoFeB single layer measured along different φ have no change, indicating that k_1 is too small to induce an anisotropic magnetization hysteresis behavior, roughly consistent with the feature of an amorphous ferromagnet. On the contrary, the magnetization hysteresis behavior of the CoFeB layer depends on φ when the CoFeB layer couples to an anisotropic FM FeRh layer. At $\varphi = 0°$ and 90°, i.e., along the easy-axis directions of the FeRh layer, the loop remains wide and square-shaped, while at $\varphi = 45°$, that is, along one of the hard-axis directions, the loop is even narrower than that in the CoFeB single layer, and the initial magnetization reversals are rounded. The loop variation with φ is further quantified through coercivity, $H_C = (H_R - H_L)/2$, H_R and H_L being coercive fields where the magnetization and field axis intersect. In other words, the coercivity in the CoFeB single layer is insensitive to φ, while it exhibits a four-pointed star pattern with φ in the CoFeB/FeRh bilayer, and each point overlaps one of the easy-axis directions of fourfold anisotropy of the FeRh layer, as shown in Fig. 3(b). Quantitatively, the coercivity in the CoFeB single layer is roughly equal to 160 Oe for $\varphi = 0°$–355°, while in the CoFeB/FeRh bilayer the coercivity has four maximum values between 240 and 260 Oe at $\varphi = 0°$, 90°, 180°, and 270°, and in between at $\varphi = 45°$, 135°, 225°, and 315°, the four minimum values of coercivity lower than ∼100 Oe are obtained. The width variation of the hysteresis loop with increasing φ is opposite to that experimentally shown in Fig. 1(b), where the widest hysteresis loop is observed at φ close to 0°. As a result, the φ dependence of coercivity depicted in Fig. 3(b) is also opposite to that presented in Fig. 1(c). Furthermore, it is apparent that the evolution of coercivity from the single layer to the bilayer, i.e., from an isotropic to an anisotropic symmetry, is attributed to the existence of the FeRh layer. In view of the fourfold symmetry, some results may be shown in the φ range from 0° to 90° only.

Next, the magnetic state (i.e., antiferromagnetism and ferromagnetism) of the FeRh layer is changed by j_2 to study its role, as shown in Fig. 4. The results show that the maximum value of coercivity appears at $\varphi = 0°$ and 90° while the minimum one is obtained at $\varphi = 45°$ for the FM FeRh. The magnetization reversal from one easy axis to the other requires a magnetic field to drive all of the moments by overcoming anisotropy energy barriers, while the moments in the FM FeRh layer yield a high magnetic viscosity, resulting in the occurrence of magnetization reversal of the CoFeB layer under a stronger magnetic field as compared to in a single CoFeB layer. It clearly demonstrates that in the CoFeB/FeRh bilayer, the cubic anisotropy of the FeRh layer can be well imprinted on the coercivity of the CoFeB layer. If the moments in the FeRh layer are FM coupled to each other, the easy-axis direction of the induced magnetic anisotropy in the CoFeB layer remains unchanged, and the coercivities close to the easy-axis directions are enhanced. Interestingly, when the CoFeB layer is coupled to an AFM FeRh layer, the widest loop emerges at $\varphi = 45°$ while the narrowest loops are obtained at $\varphi = 0°$ and 90°. In other words, the angular dependence of coercivity is preserved while the coercivity behavior with φ for the AFM FeRh layer is opposite to that in the FM FeRh layer, that is, the maximum value (slightly higher than 200 Oe) of coercivity emerges at $\varphi = 45°$ while the minimum values (∼100 Oe) are obtained at $\varphi = 0°$ and 90°. It is designated that, for the AFM FeRh layer, the easy-axis direction of the induced cubic anisotropy in the CoFeB layer can displace 45°. Therefore, the simulation results of coercivity for the AFM FeRh are qualitatively consistent with those shown in Figs. 1(b) and 1(c). When φ is close to 45° the hysteresis loops are widened, while for $\varphi = 0°$ or 90° the loops are narrow, resulting in the identical trend of H_C with φ presented in Figs. 1(c) and 4(a).

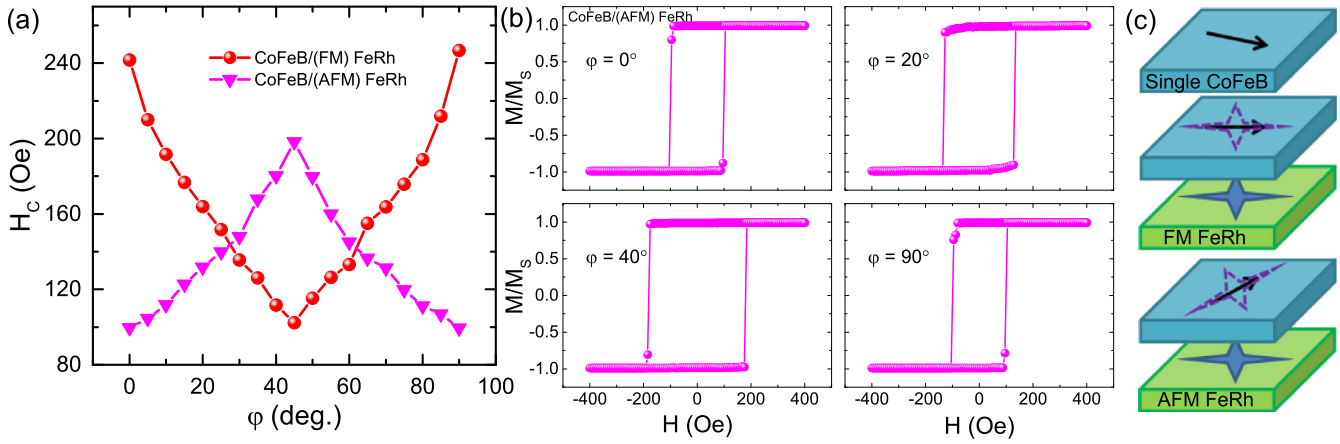

FIG. 4. (a) Calculated angular (φ) dependence of coercivity in the CoFeB layer, which is coupled to a ferromagnetic (FM) or an antiferromagnetic (AFM) FeRh layer. (b) Calculated magnetization hysteresis loops in the CoFeB/(AFM) FeRh bilayer at selected φ. (c) Schematic illustrations of virgin isotropy in the CoFeB single layer and the induced cubic anisotropy in the CoFeB/(FM) FeRh bilayer, with the easy-axis direction identical to that of the FeRh layer, and in the CoFeB/(AFM) FeRh bilayer, with a 45° deviation of the easy-axis directions from that of the FeRh layer.

To interpret the induced magnetic anisotropy in the amorphous CoFeB layer, the physical mechanism is schematically diagrammatic in Fig. 5. As shown in Fig. 5(a), the microscopic spin configurations close to the CoFeB/FeRh interface

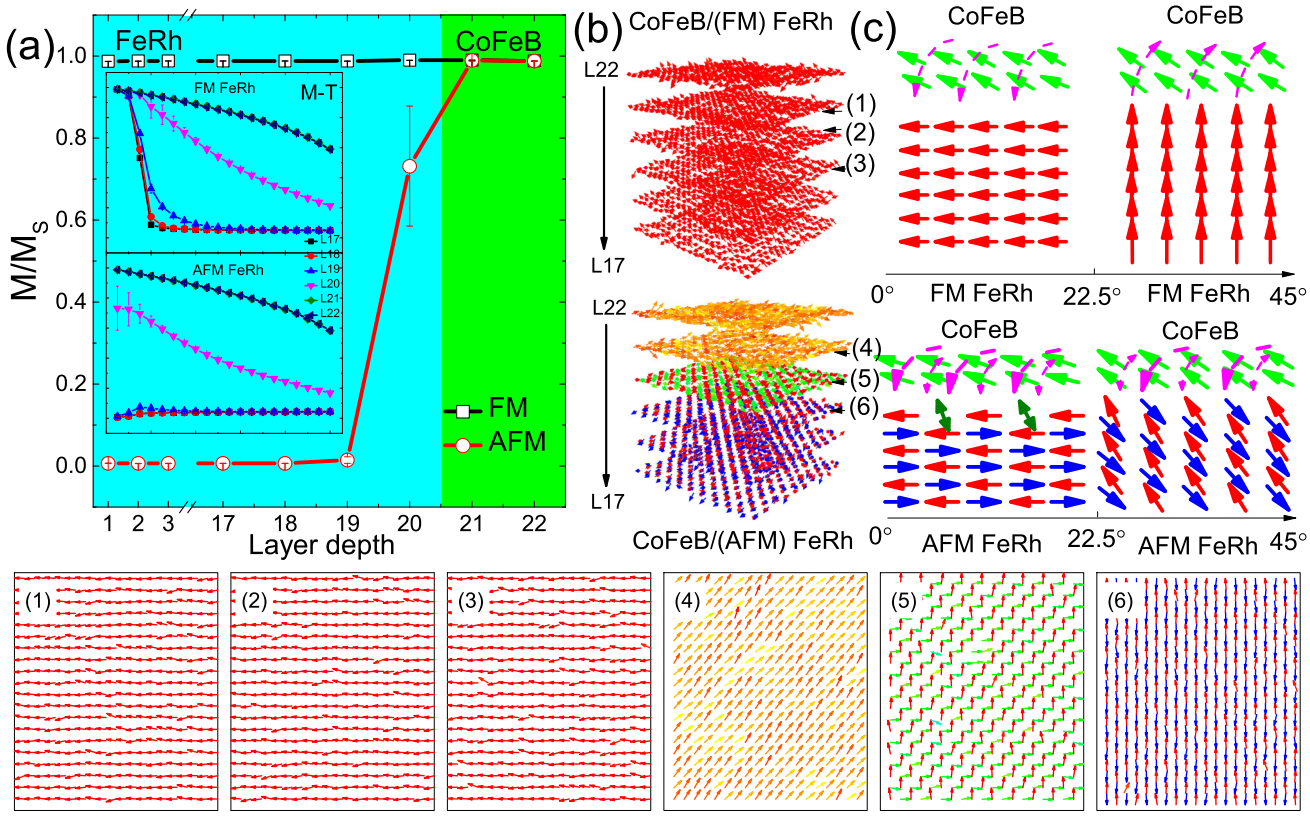

FIG. 5. (a) Magnetization of each monolayer in the CoFeB/FeRh bilayer for the FeRh layer with a ferromagnetic (FM) or an antiferromagnetic (AFM) state at low temperature after zero-field cooling, and the insets show the magnetization vs temperature (M-T) behaviors of layers 17–22 (L17–L22) in the CoFeB/FeRh bilayer for FM or AFM FeRh. (b) Microscopic spin configurations of L17–L22 in CoFeB/(FM) FeRh (upper) and CoFeB/(AFM) FeRh (bottom) bilayers, where (1)–(6) give the zoomed-in views of configurations in the selected layers. (c) Schematic illustrations of the role of the FeRh layer played on the CoFeB layer during magnetization reversal, where dashed arrows represent the dragging directions via interfacial exchange coupling, and two-headed arrows stand for two directions that are possible with equal probability.

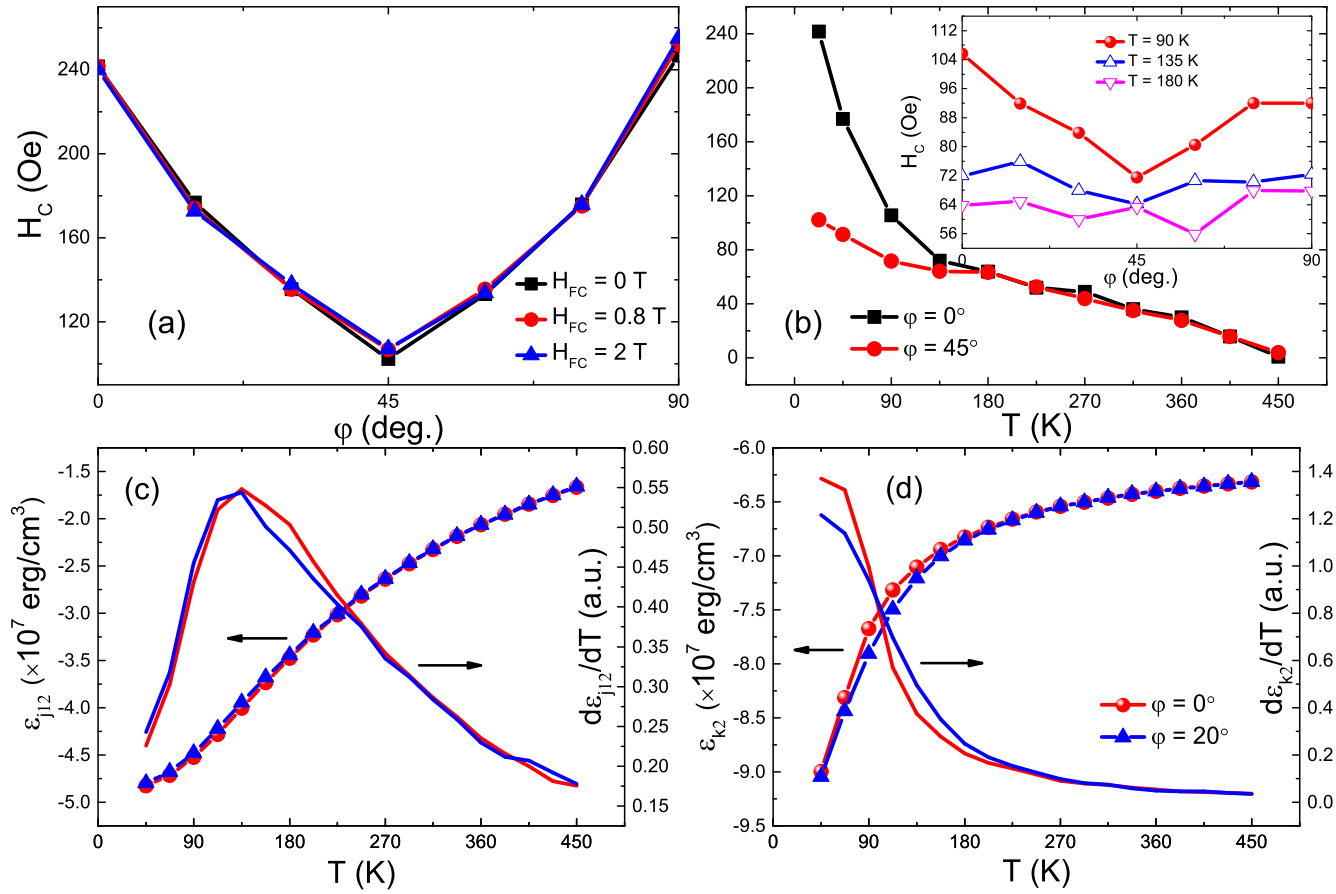

FIG. 6. (a) Calculated coercivity as a function of directional angle (φ) after cooling under selected fields (H_{FC}) in the CoFeB/(FM) FeRh bilayer. (b) Calculated coercivity as a function of temperature under zero H_{FC} at selected φ. Energy densities of (c) interfacial exchange coupling (ε_{j12}) and (d) cubic anisotropy (ε_{k2}) and their temperature derivative as a function of temperature calculated at selected φ. The inset shows the coercivity as a function of φ at selected temperatures.

are crucial for determining the magnetization reversal behaviors of the CoFeB layer. Therefore, in Fig. 5(b), the microscopic spin configurations of the monolayers close to the CoFeB/FeRh interface at low temperature after zero-field cooling are presented. For the FM FeRh layer, the moments in the CoFeB and FeRh layers are parallel, and thus the magnetization reversal of the CoFeB layer depends on the coupled moments in the FeRh layer, which may be trapped by the fourfold symmetric anisotropy. In other words, when the magnetic field is applied between 0° and 22.5°, the moments in the FeRh layer are trapped in the anisotropic well along the positive-x direction, and thus the magnetization reversal of CoFeB is impeded and coercivity is enhanced. On the contrary, with increasing magnetizing angle, the moments in the FeRh layer may be trapped in an adjacent orthogonal anisotropic well [seen in Fig. 5(c)], and the interfacial coupling encourages the magnetization reversal of the CoFeB layer under a smaller magnetic field. As a result, the coercivity decreases in the hard-axis direction of FeRh anisotropy. As the FeRh layer is AFM, in order to minimize the energies of AFM j_2 and FM j_{12} simultaneously, a canted AFM configuration is preferred at the CoFeB/FeRh interface, as (4) and (5) show in Fig. 5(b), similar to the model presented by Koon at FM/(compensated) AFM interfaces [51]. As shown in Figs. 5(b) and 5(c), at $\varphi = 0°$, some moments in a sublattice of the FeRh layer [two-headed arrows shown in Fig. 5(c)] may not work, or they may have a weak influence on the magnetization reversal of the CoFeB layer. Consequently, a weak ferromagnetism is generated on the surface of the FeRh layer to influence the magnetization reversal of the CoFeB layer in a similar manner to that at small magnetizing angles, that is, the interfacial coupling still plays a negative role on impeding the magnetization reversal of the CoFeB layer. In contrast, with increasing φ, the energy balance of the ground state after zero-field cooling is broken. Due to the tilting, all of the moments in the FeRh layer at the CoFeB/FeRh interface start to take effect upon determining the magnetization reversal of the CoFeB layer. For the antiparallel moments of the FeRh layer, the moments oriented far away from those in the CoFeB layer induce a high interfacial exchange energy to make the magnetization reversal of the CoFeB layer occur toward the nearest one of the easy-axis directions of FeRh anisotropy. Hence the coercivity along the easy-axis directions of FeRh anisotropy is the lowest, while it is the highest along the hard-axis directions.

Next, the effects of the cooling field (H_{FC}) and the temperature on the angular dependence of coercivity are studied numerically, with the results presented in Figs. 6(a) and 6(b). During cooling, thermal fluctuations are lowered and magnetic energy terms take effect one by one to determine the spin

configurations at selected temperatures. If H_{FC} is applied at high temperature, the paramagnetic moments are aligned with H_{FC}, and with decreasing temperature down to those lower than the magnetic ordering and/or freezing temperatures, the final configuration at low temperature also depends on H_{FC} [52–54]. Therefore, the H_{FC} dependence will elucidate the role that spin configuration created during cooling plays on the coercivity behavior. In Fig. 6(a), the coercivity curve with φ is almost overlapped in zero H_{FC} or $H_{FC} = 0.8$ and 2 T, indicating that the φ dependence of coercivity is not related to the spin configuration of the bilayer created after the zero-field-cooling or field-cooling process. On the other hand, different magnetic energy terms take effect at distinct critical temperatures to cause the magnetic phase transition between magnetic disordering and ordering or between free and frozen spins [39,44]. In other words, the temperature dependence may tell us which magnetic energy terms play a crucial role. The coercivity difference between $\varphi = 0^\circ$ and 45° is enhanced with decreasing temperature. At high temperature, the coercivity curves at two φ are overlapped and then splitting below $T = 180$ K. With further decreasing temperature from $T = 180$ K, the coercivity keeps increasing, while the increase of coercivity at $\varphi = 0^\circ$ faster than that at $\varphi = 45^\circ$ results in a larger splitting at lower temperature. More precisely, the φ dependence of coercivity at selected temperatures close to the splitting temperature is studied (seen in the inset of Fig. 6), and the coercivity behavior becomes fourfold symmetric below 90 K. Note that the first-order magnetic phase transition of the FeRh layer between AFM and FM states found experimentally is not taken into account in the simulation, and thus the numerical results of the temperature dependence of coercivity are distinct from those observed experimentally. However, the results of magnetic ordering and freezing with decreasing temperature governed by exchange coupling and magnetic anisotropy are still informative.

Further, as mentioned above, the in-plane anisotropic coercivity of the CoFeB layer is due to the existence of the FeRh layer. Thus the interfacial exchange energy (ε_{j12}), defined by the energy of exchange interactions between CoFeB and FeRh moments, should play a crucial role in establishing this coercivity behavior. On the other hand, the other prerequisite to obtain the in-plane imprinting of coercivity in the CoFeB/FeRh bilayer should be a strong intrinsic anisotropy in the FeRh layer. To distinguish their roles, and to demonstrate the origin of the in-plane imprinting of coercivity from the FeRh to the CoFeB layer, we present the temperature dependence of ε_{j12} and the cubic anisotropy energy (ε_{k2}) and their temperature derivative at representative φ to interpret the splitting of coercivity curves between $\varphi = 0^\circ$ and 45° at a critical temperature. The results show that ε_{j12} and ε_{k2} both decrease monotonically with decreasing temperature, while their decreases are ongoing by distinct slopes; the decrement of ε_{j12} reaches the fastest pace at $T = 135$ K, while for ε_{k2} the lower the temperature is, the faster is the decrement. The peak of $d\varepsilon_{j12}/dt$ designates that the most drastic reconstruction of magnetic ordering happens, resembling a magnetic phase transition between paramagnetic and ferromagnetic states. On the other hand, the continuous decrease in ε_{k2} at low temperature stands for the freezing of moments. By comparing the temperature dependence of coercivity and magnetic energies, apparently, in the pinning state of moments in the FM FeRh layer, the fourfold symmetric coercivity phenomenon is observed only when the interfacial exchange coupling takes effect. In other words, the interfacial exchange coupling, other than the spin configuration, is crucial for the imprinting of cubic anisotropy on the amorphous CoFeB layer.

Finally, the universality of this kind of induced anisotropy imprinted through interfacial exchange coupling is studied. At this point, the CoFeB layer and its uniaxial anisotropy are both preserved, while the cubically anisotropic FeRh layer is replaced by another, namely a uniaxially anisotropic hard-magnet layer with unchanged k_2 magnitude. The easy axis is set along 45° or 90° with respect to the positive x-direction, and the hysteresis loop and coercivity results are depicted in Fig. 7. For the 45° easy axis, labeled by 45° EA, the widest and square loop is obtained at $\varphi = 45^\circ$, while the narrowest and rounded loop appears at $\varphi = 0^\circ$ and 90°. On the contrary, if the hard-magnet layer with an easy-axis direction is in-plane orthogonal to that of the CoFeB layer, i.e., 90° EA, the narrowest hard-axis loop appears at $\varphi = 0^\circ$, and with increasing φ to 90°, the loop width is increasing and the loop shape is of rectangularity. In the φ range from 0° to 355°, the easy-axis distribution and coercivity are given. Interestingly, the anisotropy can also be imprinted on the amorphous CoFeB layer, corresponding to the angular dependence of coercivity in the CoFeB layer, and it remains uniaxial as well, with the direction well overlapping the easy-axis direction of the hard-magnet layer. Hence, the imprinting of a hard-magnet anisotropy on a soft-magnet layer through interfacial exchange coupling is suitable for both cubic and uniaxial symmetries.

V. CONCLUSION

In summary, an in-plane fourfold magnetic anisotropy, characterized by the angular dependence of coercivity, was obtained in the amorphous CoFeB layer of the CoFeB/FeRh bilayer system, which should be of weak ferromagnetism with uniaxial anisotropy. The maximum values of coercivity in the CoFeB layer overlap the easy-axis directions of the in-plane fourfold anisotropy for the FM FeRh layer, despite an in-plane 45° deviation from the anisotropy direction of the AFM FeRh layer. By means of Monte Carlo simulation, the cooling field dependence of coercivity excludes the role of spin configuration; meanwhile, the temperature dependence of coercivity, and the exchange and anisotropy energies, have demonstrated the crucial role of interfacial exchange coupling in the process of imprinting the anisotropy. Finally, we suggest that this imprinting mechanism of anisotropy through interfacial exchange coupling is also applicable for different types of magnetocrystalline anisotropies. This work provides strong evidence that the induced anisotropy in a soft-magnet layer depends strongly on interfacial exchange coupling, and reveals the mechanism of the magnetic state governed easy-axis direction of the induced anisotropy. Our results indicate a pathway to engineer the formation and controllability of magnetic anisotropy in soft-magnet materials for the achievement of writing, processing, and reading functionalities in ultradense information storage as well as in different types of purely solid-state spin-based information-processing devices.

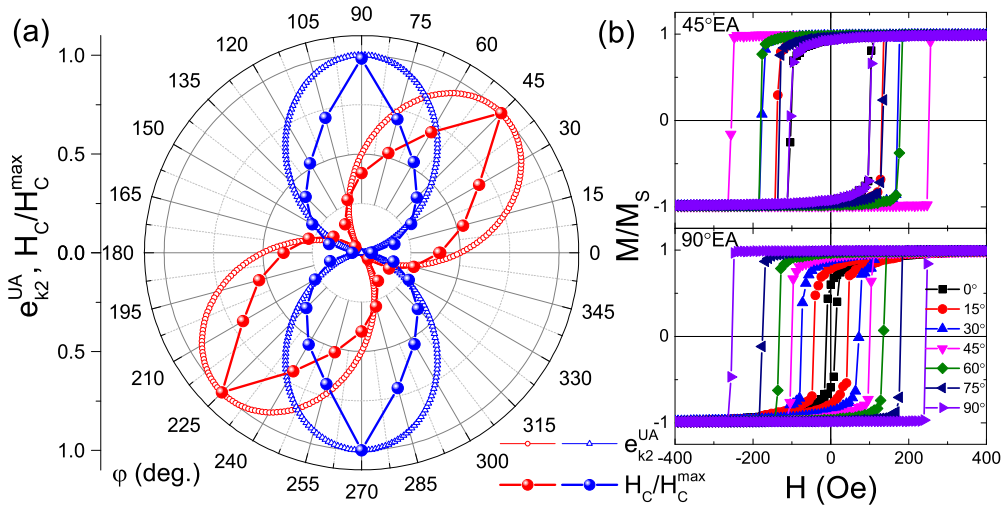

FIG. 7. (a) Unit vector of the easy axis of uniaxial anisotropy (open symbols) and angular (φ) dependence of the normalized coercivity (solid symbols) in the CoFeB layer, which is coupled to a hard-magnet FM layer with strong uniaxial anisotropy along selected easy-axis directions. (b) Calculated magnetization hysteresis loops of the CoFeB layer, which is coupled to the hard-magnet FM layer with uniaxial anisotropy along the 45° and 90° easy-axis directions with respect to the positive x-direction, at selected φ.

ACKNOWLEDGMENTS

This work was supported by National Natural Science Foundation of China (11774045, 11874150, 51871233), Joint Research Fund Liaoning-Shenyang National Laboratory for Materials Science (20180510008), Ningbo Natural Science Foundation (2019A610054), and Fundamental Research Funds for Central Universities (N182410008-1).

[1] F. Radu and H. Zabel, Exchange bias effect of ferro-/antiferromagnetic heterostructures, in *Magnetic Heterostructures: Advances and Perspectives in Spinstructures and Spintransport*, edited by H. Zabel and S. D. Bader (Springer, Berlin, 2008), pp. 97–114.

[2] J. Nogués and I. K. Schuller, J. Magn. Magn. Mater. **192**, 203 (1999).

[3] J. Nogués, J. Sort, V. Langlais, V. Skumryev, S. Suriñach, J. S. Muñoz, and M. D. Baró, Phys. Rep. **422**, 65 (2005).

[4] A. E. Berkowitz and R. H. Kodama, Exchange anisotropy, in *Nanomagnetism: Ultrathin Films, Multilayers and Nanostructures*, edited by D. L. Mills and J. A. C. Bland (Elsevier B.V., the Netherlands, 2006), pp. 115–152.

[5] P. K. Manna, S. M. Yusuf, M. Basu, and T. Pal, J. Phys.: Condens. Matter **23**, 506004 (2011).

[6] M. J. Zuckermann, Solid State Commun. **12**, 745 (1973).

[7] P. J. Jensen, H. Dreyssé, and M. Kiwi, Eur. Phys. J. B **46**, 541 (2005).

[8] C. L. Chien and D. H. Reich, J. Magn. Magn. Mater. **200**, 83 (1990).

[9] P. K. Manna and S. M. Yusuf, Phys. Rep. **535**, 61 (2014).

[10] D. Lederman, J. Nogués, and I. K. Schuller, Phys. Rev. B **56**, 2332 (1997).

[11] S. Bedanta and W. Kleemann, J. Phys. D **42**, 013001 (2009).

[12] S. Chikazumi, *Physics of Ferromagnetism* (Oxford University Press, New York, 2010).

[13] J. M. D. Coey, *Magnetism and Magnetic Materials* (Cambridge University Press & Peking University Press, Cambridge, 2014).

[14] W. Zhang, Y. Zhai, M. Lu, B. You, H. R. Zhai, and C. G. Morgan, Chin. Phys. B **24**, 047502 (2015).

[15] P. K. Manna, E. Skoropata, Y. W. Ting, K. W. Lin, J. W. Freeland, and J. Van Lierop, J. Phys.: Condens. Matter **28**, 486004 (2016).

[16] R. C. Hall, J. Appl. Phys. **30**, 816 (1959).

[17] K. Abe, Y. Miyamoto, and S. Chikazumi, J. Phys. Soc. Jpn. **41**, 1894 (1976).

[18] Y. Hu, X. Li, X. Chi, A. Du, and F. Shi, J. Phys. D **51**, 055001 (2018).

[19] D. Gozzi, A. Latini, G. Capannelli, F. Canepa, M. Napoletano, M. R. Cimberle, and M. Tropeano, J. Alloys Compd. **419**, 32 (2006).

[20] T. Hu, X. Chi, Q. Lu, L. Yu, R. Li, Y. Liu, A. Du, Z. Li, F. Shi, and Y. Hu, J. Alloys Compd. **801**, 465 (2019).

[21] N. Miyata, J. Phys. Soc. Jpn. **16**, 1291 (1961).

[22] R. F. Penoyer and M. V. Shafer, J. Appl. Phys. **30**, S315 (1959).

[23] R. F. Pearson, J. Appl. Phys. **33**, 1236 (1962).

[24] M. E. McHenry, Magnetic steels, in *Encyclopedia of Materials: Science and Technology*, edited by K. H. J. Buschow, R. W. Cahn, M. C. Flemings, B. Ilschner, E. J. Kramer, S. Mahajan, and P. Veyssière (Elsevier, the Netherlands, 2001), pp. 4961–4964.

[25] J. Wolf, K. Kiefer, M. C. Rheinstädter, K. Knorr, and M. Enderle, Eur. Phys. J. B **22**, 461 (2001).

[26] B. N. Engel, C. D. England, R. A. Van Leeuwen, M. H. Wiedmann, and C. M. Falco, Phys. Rev. Lett. **67**, 1910 (1991).

[27] D. Suess, J. Fidler, G. Zimanyi, T. Schrefl, and P. Visscher, Appl. Phys. Lett. **92**, 173111 (2008).

[28] K. Lenz, S. Zander, and W. Kuch, Phys. Rev. Lett. **98**, 237201 (2007).

[29] B. Y. Wang, C. C. Chiu, W. C. Lin, and M. T. Lin, Appl. Phys. Lett. **103**, 042407 (2013).
[30] M. Grimsditch, A. Hoffmann, P. Vavassori, H. Shi, and D. Lederman, Phys. Rev. Lett. **90**, 257201 (2003).
[31] H. Ohldag, H. Shi, E. Arenholz, J. Stöhr, and D. Lederman, Phys. Rev. Lett. **96**, 027203 (2006).
[32] I. Suzuki, Y. Hamasaki, M. Itoh, and T. Taniyama, Appl. Phys. Lett. **105**, 172401 (2014).
[33] N. T. Nam, W. Lu, and T. Suzuki, J. Appl. Phys. **105**, 07D708 (2009).
[34] O. V. Billoni, S. A. Cannas, and F. A. Tamarit, J. Phys.: Condens. Matter **23**, 386004 (2011).
[35] D. Suess, M. Kirschner, T. Schrefl, W. Scholz, R. Dittrich, H. Forster, and J. Fidler, J. Appl. Phys. **93**, 8618 (2003).
[36] D. Suess, M. Kirschner, T. Schrefl, J. Fidler, R. L. Stamps, and J. V. Kim, Phys. Rev. B **67**, 054419 (2003).
[37] M. Kirschner, D. Suess, T. Schrefl, J. Fidler, and J. N. Chapman, IEEE Trans. Magn. **39**, 2735 (2003).
[38] Y. Hu, Nanotechnology **30**, 025708 (2019).
[39] R. Li, L. Yu, and Y. Hu, Phys. Status Solidi RRL **13**, 1900039 (2019).
[40] X. Chi and Y. Hu, Nanotechnology **31**, 125703 (2020).
[41] Q. F. Zhan, W. Zhang, and K. M. Krishnan, Phys. Rev. B **83**, 094404 (2011).
[42] Q. Zhan and K. M. Krishnan, J. Appl. Phys. **107**, 09D703 (2010).
[43] W. Zhang, M. E. Bowden, and K. M. Krishnan, Appl. Phys. Lett. **98**, 092503 (2011).
[44] Y. Hu, T. Hu, X. Chi, Y. Wang, Q. Lu, L. Yu, R. Li, Y. Liu, A. Du, Z. Li, and F. Shi, Appl. Phys. Lett. **114**, 023903 (2019).
[45] A. Fernández-Pacheco, E. Vedmedenko, F. Ummelen, R. Mansell, D. Petit, and R. P. Cowburn, Nat. Mater. **18**, 679 (2019).
[46] S. Ikeda, K. Miura, H. Yamamoto, K. Mizunuma, H. D. Gan, M. Endo, S. Kanai, J. Hayakawa, F. Matsukura, and H. Ohno, Nat. Mater. **9**, 721 (2009).
[47] L. H. Lewis, C. H. Marrows, and S. Langridge, J. Phys. D **49**, 323002 (2016).
[48] N. Mohanta, E. Dagotto, and S. Okamoto, Phys. Rev. B **100**, 064429 (2019).
[49] J. d'Albuquerque e Castro, D. Altbir, J. C. Retamal, and P. Vargas, Phys. Rev. Lett. **88**, 237202 (2002).
[50] M. Charilaou and F. Hellman, J. Appl. Phys. **117**, 083907 (2015).
[51] N. C. Koon, Phys. Rev. Lett. **78**, 4865 (1997).
[52] J. Nogués, D. Lederman, T. J. Moran, and I. K. Schuller, Phys. Rev. Lett. **76**, 4624 (1996).
[53] Y. Hu and A. Du, J. Appl. Phys. **102**, 113911 (2007).
[54] W. B. Rui, Y. Hu, A. Du, B. You, M. W. Xiao, W. Zhang, S. M. Zhou, and J. Du, Sci. Rep. **5**, 13640 (2015).